AN ULTRA-LOW-POWER PHYSICS PACKAGE FOR A CHIP-SCALE ATOMIC CLOCK

Mark J. Mescher*, Robert Lutwak†, and Mathew Varghese*
*Charles Stark Draper Laboratory, †Symmetricom Inc.

ABSTRACT

We report the design and measured thermal and mechanical performance of an ultra-low-power physics package for a Chip-Scale Atomic Clock (CSAC). This physics package will enable communications and navigation systems that require a compact, low-power atomic frequency standard. The physics package includes a unique combination of thermal isolation, mechanical stability and robustness, and small package volume. We have demonstrated temperature control at a nominal operating temperature of 75°C in a room-temperature, vacuum ambient requiring only 7mW of heating power. This represents a power reduction of over two orders of magnitude compared to the lowest-power existing commercial technology [1] and more than an order of magnitude improvement over other CSAC development efforts [2].

Keywords: atomic clock, low-power, thermal isolation, polyimide suspension

INTRODUCTION

Atomic clocks play an essential role in the timing and synchronization of modern communication and navigation systems. To date, however, the relatively large size and power consumption (125 cm^3 and 6 Watts) of atomic clocks have prevented their application in portable devices. The authors are developing a chip-scale atomic clock, with size < 1 cm^3 and power < 30mW, which will enable high-performance timing technologies in portable, handheld devices.

Conventional gas cell atomic clocks employ an architecture which has been refined over 40 years of use in commercial and military applications. An alkali-metal vapor, typically rubidium, is created in a heated cell. The cell is contained in a microwave cavity with a resonance corresponding to the transition energy between two of the ground-state hyperfine levels of the rubidium atom. The cell is illuminated by a rubidium discharge lamp and the transmission through the atomic vapor is monitored on a photodetector. Microwaves at the hyperfine frequency of rubidium (6.8 GHz) are synthesized from a quartz RF oscillator and applied to the microwave cavity. In operation, the light from the discharge lamp optically pumps the rubidium in the resonance cell into one of the two ground states. When tuned to the hyperfine frequency, microwaves applied to the cavity redistribute the atomic states, producing a relative decrease in the transmitted light. This resonance signal is used to servo the frequency of the quartz oscillator to the atomic transition frequency, thereby producing a highly stable oscillator. The size and power consumption of these systems remain too high for portable battery-powered applications. The lamp typically requires more than one watt of power and the microwave cavity must have a size of order centimeters. Both the lamp and resonance cavity/cell assembly must be independently temperature-stabilized at temperatures close to 100 °C.

We (Symmetricom, Draper Laboratory, and Sandia National Laboratories), have developed an alternative implementation based on the method of coherent population trapping [3]-[5]. The power hungry resonance lamp of the conventional architecture is replaced by a low-power Vertical Cavity Surface Emitting Laser (VCSEL) which dissipates less than two milliwatts of power. The cesium cell is of millimeter- rather than centimeter-scale. The VCSEL is integrated with the Cs cell in a "folded-optics" configuration as shown in Figure 1. Emitted light passes through the cell and is reflected by a mirror on the opposite side of the cell back to a photodiode which is integrated on the VCSEL die. The VCSEL is tuned to the D1 optical transition of cesium at λ=894 nm and directly modulated at $\nu_{HF}/2$ = 4.6 GHz, where ν_{HF} is the hyperfine transition frequency of cesium. The cell and VCSEL are temperature-stabilized at approximately 75°C to optimize clock performance [4].

The cell and VCSEL are supported by a novel suspension system that relies on the strength and low thermal conductivity of polyimide to minimize conductive thermal losses from the heated resonance cell while providing mechanical stability and isolation from external vibration. The suspension structure consists of upper and lower halves (Figure 1).

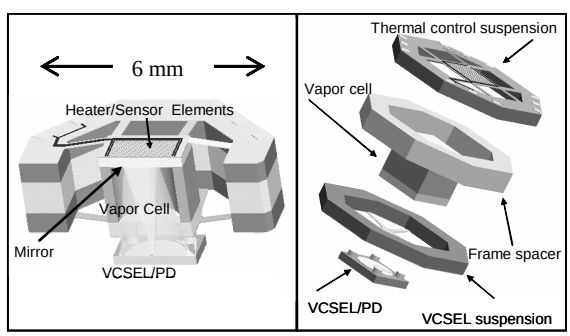

Figure 1. (Left) Cross section view of physics package without LCC, and (right) exploded view.

Each half consists of a silicon frame that supports multiple polyimide tethers converging on a central attachment plate. During assembly, the two central attachment plates mount to opposite sides of the vapor cell, while the two frames are mounted on opposite sides of a spacer. The spacer and the cell thickness are such that the tethers are stretched out of plane in the assembly process. The introduction of a small angle in the tethers greatly stiffens the suspension structure by eliminating low-frequency bending modes in the suspension beams, thus z-axis motion of the cell causes the tethers to stretch rather than bend.

The superior thermal isolation and mechanical stiffness provided by the suspension structure is made possible through appropriate material choice and packaging techniques. Polyimide has extremely low thermal conductivity (0.2 W/m°C) that minimizes conduction heat loss and permits compact suspension designs by reducing required beam lengths. In addition, similar to other polymers, it has a high yield strain (3%) which enables the angled suspension system to be built from components that are fabricated using planar, batch-fabrication processes. In addition, the electrical leads to the heated components may be directly patterned onto the polyimide.

FABRICATION

Cell Fabrication

The $(2\ \text{mm})^3$ cesium resonance cell is fabricated of silicon with anodically-bonded Pyrex® windows. Details of the cell fabrication and cesium loading have been described previously [5]. A quarter-waveplate necessary for circular polarization is attached to the tablet after cesium filling but prior to dicing (Figure 2).

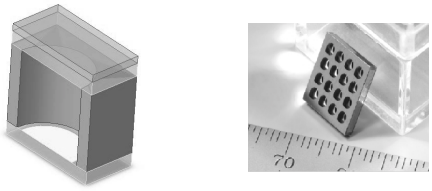

Figure 2. (left) Cross section model of cesium vapor cell including waveplate, and (right) 4x4 tablet ($1\ \text{cm}^2$) of Si cells before cesium loading and tablet dicing.

Suspension Fabrication

The upper (thermal control) and lower (VCSEL/PD) portions of the suspension structure are fabricated similarly on separate silicon wafers. The frame spacer is conventionally machined from aluminum. The patterned polyimide layers that form the suspension tethers are identical except for a 1.5mm hole in the center plate of the VCSEL suspension that allows optical transmission of the laser source and collected light. The process sequences are identical except for the metallization. These are outlined in Table 1. Figure 3 shows a fabricated assembly.

Table 1. Suspension structure fabrication sequence.

Grow etch stop for backside silicon etch: Thermal SiO_2 (1.0 μm)
Spin on suspension structural material: Photodefined polyimide (5 μm)
Sputter thermal control suspension metal: Ti/Pt (0.03μm/0.25μm)
Sputter VCSEL/PD suspension metal: Ti/Pt/Au/Ti (0.03μm/0.4μm/0.4μm/0.1μm)
Sputter bond pad metal: Ti/Au (0.03μm/0.5μm)
Etch Si (DRIE) for suspension release: through wafer (500μm)
Plasma-etch thermal oxide etch-stop layer.

Assembly and Packaging

The cell and suspension structures are assembled with epoxy. EPO-TEK® 353ND is used for its optical transmission characteristics and its low outgassing properties. An exploded view before assembly is depicted in Figure 1. Individual cells are mounted in the suspension structure. The thermal control suspension structure is placed face-down in an alignment fixture. The cell is mounted mirror-side down on the central attachment plate of the suspension via manual dispensing of epoxy. After curing the adhesive interface thickness is 5μm. The aluminum frame spacer is then aligned via fiducial marks and adhered to the silicon frame similarly. Finally the VCSEL/PD suspension is aligned using another fiducial mark on the frame. Epoxy attaches the center plate to the cell and the frame to the frame spacer.

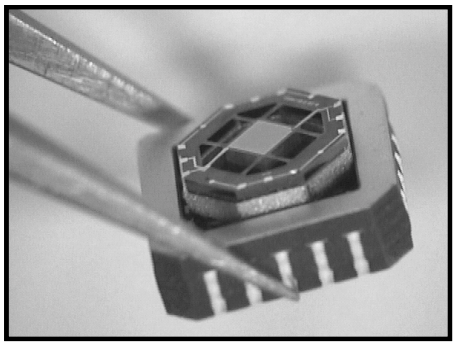

Figure 3. Fabricated physics package assembly mounted in an LCC (thermal control side facing up).

The VCSEL/PD die is attached to the cell via solder reflow. 0.018inch solder balls are first attached to the VCSEL/PD pads. The VCSEL/PD solder balls are aligned to pad locations on the center plate of the VCSEL/PD suspension and attached by reflowing the solder. Simultaneously solder balls are attached to pads on the frame of the VCSEL/PD suspension to enable mounting of the frame assembly to a ceramic leadless chip carrier (LCC). The LCC is then aligned and a final reflow done to connect the frame pads to those of the LCC. The heater and temperature sensor are connected via wire bond to corner pads in the LCC. Finally, an alumina lid, containing an activated getter, is attached in vacuum. A solder preform is mounted onto the seal-ring of the LCC and reflowed to seal the device. Including the vacuum package, the overall size of the phsyics package is approximately 0.6 cm^3.

PERFORMANCE CHARACTERISTICS

Thermal Control

The cell temperature is maintained through integrated single-element resistive platinum temperature-sensing and heating elements, both of which are patterned directly onto the central polyimide plate of the thermal control side of the suspension structure. Measured temperature coefficients of resistance for the sputtered films are 2300ppm/°C with a 4% variation across a 4" in wafer. The temperature sensor is distributed uniformly across the cell face to provide an accurate average temperature measurement of the vapor cell. The portion of the trace which runs along the suspension tether from the center plate to outer frame bond pad is designed to have relatively low resistance (0.9% in current devices) to prevent partial sensing of the frame (i.e. ambient) temperature. The sense resistor is sized (10kΩ) to achieve approximately 0.1°C temperature sensitivity with low-power readout electronics. The heater resistance is distributed around the periphery of the cell rather than uniformly across the plate surface. This provides a more uniform temperature because most of the heat transfer away from this surface is through the silicon walls of the cell to all cell faces, which then radiate heat to the LCC package. The heater resistance is sized (400Ω) such that power is delivered efficiently from the control electronics (3 V supply) while still maintaining sufficient voltage overhead to provide fast device turn-on and good control response. In the case of the heater, the tether traces contribute to inefficiency by heating the tethers and the frame (7.5% in current devices). Both the heating and sensing resistors are configured such that current flowing through one segment of the resistor is balanced by a current in another segment in close proximity that is flowing in the opposite direction, which minimizes magnetic fields in the vicinity of the vapor cell.

Heat loss to the frame and package occur through radiation, gas conduction and convection, and conduction in the suspension tethers. Gaseous conduction and convection are eliminated by vacuum packaging the device. However, even at atmospheric pressure, convection is suppressed due to the small size of the gap between the heated device and the LCC package. Radiation is driven by surface area and emissivity. Gas conduction is driven by gap dimensions, gas composition and pressure. The bulk conduction is determined by thermal conductivity and shape and size of the suspension tethers and their metal interconnect. Detailed models of radiation must account for the multiple surface emissivities and shape factors of the system. However, the heated Cs cell will have radiative heat loss with a temperature dependence given by

$$P = \varepsilon \cdot \sigma \cdot A_{cell} \cdot \left(T_{cell}^4 - T_{amb}^4\right)$$

where ε is a parameter which embodies the relative emissivities of the cell and heat-reflecting package, A_{cell} is the surface area of the cell, and σ is the Stefan-Boltzmann constant. As a general rule, heat loss by thermal radiation is reduced by minimizing the cell's surface area and average emissivity. The cell has four saw-diced silicon surfaces, one polyimide-and-platinum-covered surface and one surface of GaAs (the VCSEL/PD). These materials all have emissivities around 0.5, with variation depending on surface finish. Some materials, such as polished aluminum, can have emissivities as low as 0.03. While we have not yet implemented surface coatings on the cell sidewalls to reduce radiation, we have conducted experiments with test aluminum cells in place of the standard cell which indicate that even lower heater power requirements are possible (Figure 4).

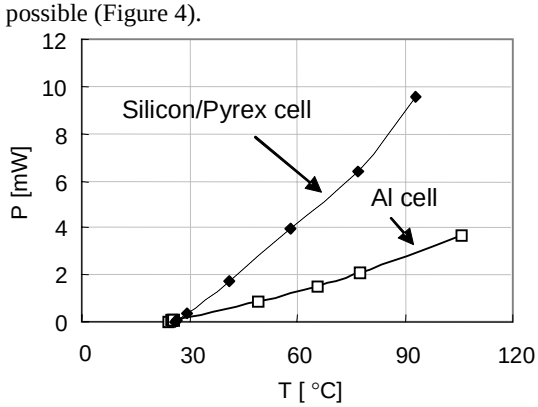

Figure 4. Measured steady state heater power as a function of cell temperature in a vacuum ambient (24°C, 2mTorr) for a silicon/pyrex cell and a low-emissivity polished aluminum test cell.

Heat loss due to gas conduction was characterized to determine how package vacuum level affects required heater power. Figure 5 shows heater power for a cell held at 80 °C in 24 °C ambient as a function of gas

(air) pressure. For low pressures (less than about 20mTorr) the power is dominated by radiation. For intermediate pressures, heat transfer is molecular and is proportional to pressure. At high pressures the heat transfer is essentially independent of pressure and depends on the thermal conductivity of the gas.

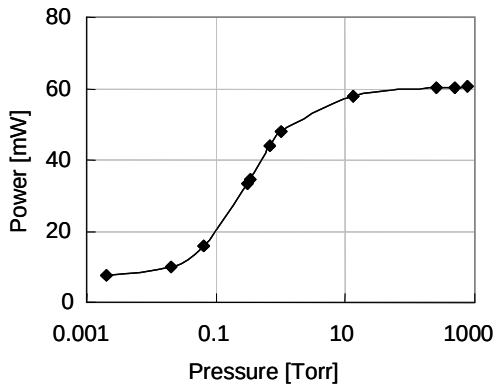

Figure 5. Heater power required to maintain cell temperature at 80°C in a 24°C ambient of varying pressure. Experiment was performed in a bell jar with the device packaged as shown in Figure 3.

The solid material conduction losses in our CSAC physics package are currently not measurable and are small compared to radiation losses. The predicted power loss at 75°C by conduction is 0.9mW, or 13% of the total. The specifications and predicted thermal performance characteristics of the suspension system are shown in Table 2.

Table 2. Tether system design values.

Total tether count	16
Polyimide tether	5x375x1000µm
VCSEL/PD metal widths	10µm
Heater metal trace widths	80µm
Sensor metal trace widths	30µm
Thermal Resistances:	
Polyimide tethers (total)*	167°C/mW
Metal traces (total) †	87°C/mW
Total	57°C/mW

* 0.2 W/m°C polyimide conductivity assumed
† bulk conductivity values assumed

The heat capacity of the system was also estimated from a time constant. The step response used in the estimate is shown in Figure 6. The measured time constant was 63 seconds. From the steady state measurements shown in Figure 4, the effective total thermal resistance (radiation-dominated) at 75°C is approximately 6.3°C/mW, which yields a heat capacity of 0.010 J/C. This is within 5% of the calculated value.

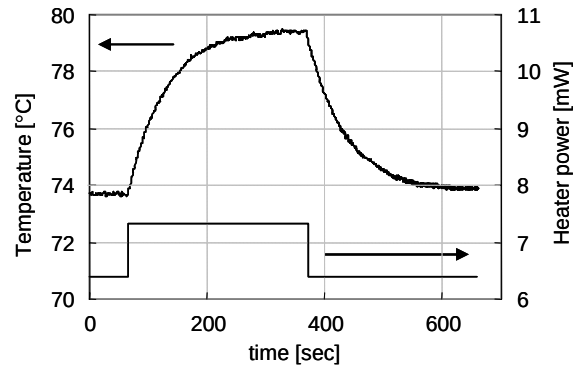

Figure 6. Measured thermal step response of physics package.

Mechanical Design

As described earlier, the mechanical design takes advantage of several material properties of polyimide to meet the conflicting design requirements of low heat loss and mechanical rigidity while permitting planar MEMS batch fabrication techniques for the suspension system. We describe the design in the context of two mechanical specifications: fundamental mechanical resonance frequency and maximum sustainable steady acceleration ("g" load) without plastic deformation of the polyimide tethers.

Figure 7 shows a cross-section of one half of the suspension system. As is suggested by the figure, the tethers are dominated by axial rather than bending stresses. They are more appropriately thought of as cables rather than bending beams. If one considers only z-axis forces, the system is equivalent to the mass-spring model shown in Figure 7, where d is the spring's displacement from equilibrium after assembly (both springs are nominally in tension). For large z-displacements, these springs are highly non-linear.

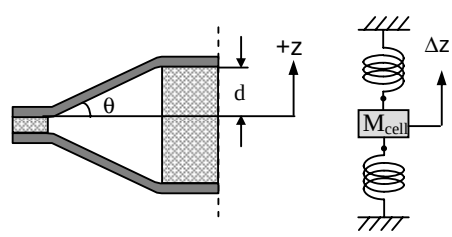

Figure 7. Depiction of (left) cross section of half-device showing exaggerated tether angle, and (right) linearized mass-spring model.

In order for the tethers to act as springs, they must be in tension at all times. Under this condition the small signal resonant frequency of the suspension system is independent of the magnitude of the tensile stress. It is

the angle of the tethers rather than the pre-tension that sets the resonant frequency. However, if the stress in the tethers turns compressive at any point, they buckle and do not provide any significant mechanical support. Such a condition is encountered under a high static "g" load and is described later. The restoring force of a single tether for a displacement z is

$$F = -\frac{E \cdot A \cdot z}{L} \cdot \left(1 - \frac{L}{\sqrt{L^2 + z^2}}\right)$$

This equation is non-linear in z, but for small motions Δz around the equilibrium displacement, d, a linear equation for the total restoring force in the z-direction can be used:

$$F_T = -N \cdot k \cdot \Delta z$$

Here N is the total tether count and k is the linearized spring constant of a single tether:

$$k = \frac{E \cdot A}{L} \cdot \left[1 - \left(\frac{L}{\sqrt{L^2 + d^2}}\right)^3\right] = \frac{E \cdot A}{L} \cdot \left[1 - \left(\cos\left(\theta_0\right)\right)^3\right]$$

E is elastic modulus, A is tether cross sectional area, L is tether length, and θ_0 is the as-built tether angle (Figure 7). This spring constant greatly exceeds that of the bending stiffness for even modest angles. The resonant frequency is now given by the familiar relation:

$$f_{res} = \frac{1}{2 \cdot \pi} \cdot \sqrt{\frac{N \cdot k}{M_{cell}}}$$

It should be noted that x- and y-axis resonance frequencies can be calculated simply by replacing $\cos(\theta_0)$ with $\sin(\theta_0)$ in the equation for spring constant. It follows from this that resonant frequencies and maximum "g" loads are higher in the x and y directions.

Test units with a range of built-in tether angles were built and tested to validate the model. A small magnetically permeable disk was attached to the cell in these test units and excited by a miniature electromagnet. Displacement was measured with an interferometer as the excitation frequency was swept manually. Fundamental mode resonances were calculated by fitting the data to a standard mass-spring-damper model. Measured resonant frequency data was estimated to be accurate to better than 1%. The results are compared to the model in Figure 8. The elastic modulus assumed for the model was 3.5GPa. The mass of the cell and attached magnetic disk is estimated at 27milligrams, significantly greater than the cell alone (18milligrams). Thus, the resonant frequency of real devices is expected to be higher by the square root of the mass ratio of the test unit and real device $(27mg/18mg)^{0.5}$ for the same tether angle. This predicts a resonant frequency of 2450Hz for a real device with tether angle of 10 degrees.

In order to calculate the maximum "g" load of the devices, we estimate the forces present at the yield strain, $\varepsilon_{max,}$ of the tethers. Under steady acceleration, the maximum g-load, A_{max}, can be expressed as

$$A_{max} = \frac{N \cdot E \cdot A}{2 \cdot M_{cell}} \cdot \sqrt{\varepsilon_{max}^3 \cdot \left(2 + \varepsilon_{max}\right)}$$

We assume that the cell has been displaced such that only the upper or lower halves of the suspension system remain in tension and thus provide mechanical support. For ε_{max} = 0.03, $A_{.max}$ = 2200g's (1500g's rms).

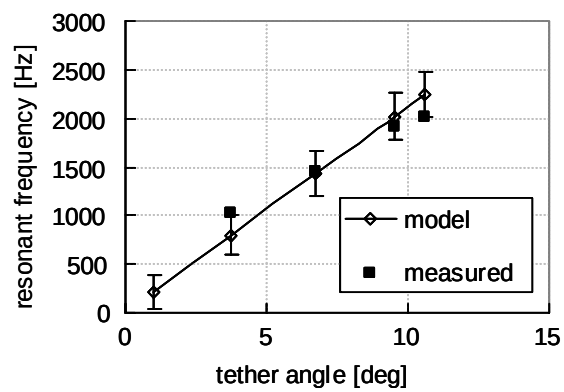

Figure 8. Measured and modeled mechanical resonance frequency as a function of as-built tether angle. The error bars are attached to the theoretical curve: they are based on estimates of fabrication tolerances including cell mass, tether dimensions and tether angle.

CONCLUSIONS

We reported on the design and measured thermal and mechanical performance of an ultra-low-power physics package for a Chip-Scale Atomic Clock (CSAC). We have demonstrated temperature control at a nominal operating temperature of 75°C in a room-temperature, vacuum ambient requiring only 7mW of heating power. Lowering the cell's emissivity has been experimentally demonstrated to provide further power reduction. Measured resonance frequency corresponding to 2.5kHz for a physics package was presented. In addition, models of the suspension system indicate that the physics package can sustain maximum "g" loads in excess of 2000g without damage.

ACKNOWLEDGEMENTS

The authors wish to thank Mike Garvey of the Symmetricom TRC and John McElroy of Draper Laboratory for supporting and directing this effort. We are also thankful for the technical and theoretical support provided by Gary Tepolt, John LeBlanc, and Amy Duwel of Draper Laboratory, Don Emmons and Peter Vlitas of the Symmetricom TRC, and Darwin Serkland of Sandia National Laboratories. We thank Yen-Wah Ho, Greg Romano, Ryan Prince, Maria Cardoso, Maria Holmboe, Katherine Ashton, and Bessy Silva for assistance in the fabrication and assembly of physics package components. We also thank V. M. Montano and A. T. Ongstad for assistance in the fabrication of the VCSEL/RCPD chips and T. W. Hargett for assistance in the epitaxial semiconductor growth. This work is supported by the Defense Advanced Research Projects Agency, Contract # NBCHC020050.

REFERENCES

[1] X-72 Data Sheet, *http://www.symmetricom.com /media/pdf/documents/ds-x72.pdf*

[2] J. Kitching, "Chip Scale, Microfabricated Atomic Clocks (An emerging technology)" 29th Annual Time and Frequency Metrology Seminar, NIST, Boulder, CO, June 14 - June 17, 2004.

[3] R. Lutwak, et. al., "The Chip-Scale Atomic Clock – Coherent Population Trapping vs. Conventional Interrogation", *Proceedings of the 34th Annual Precise Time and Time Interval (PTTI) Systems and Applications Meeting*, December 3-5, 2002, Reston, VA, pp. 539-550.

[4] R. Lutwak, et. al., "The Chip-Scale Atomic Clock – Recent Development Progress", *Proceedings of the 35th Annual Precise Time and Time Interval (PTTI) Systems and Applications Meeting*, December 2-4, 2003, San Diego, CA, pp. 467-478.

[5] R. Lutwak, Jinquan Deng, W. Riley, M. Varghese, M. Mescher, D. K. Serkland and G. M. Peake, "The Chip-Scale Atomic Clock – Recent Development Progress", *Proceedings of the 36th Annual Precise Time and Time Interval (PTTI) Systems and Applications Meeting*, December 7-9, 2004, Washington, DC.

[6] L-A. Liew, et. al. "Microfabricated alkali atom vapor cells," *Applied Physics Letters*, **84**, p. 2694 (2004).